

Learning in ImaginationLand: Omnidirectional Policies through 3D Generative Models (OP-Gen)

Yifei Ren¹ and Edward Johns¹

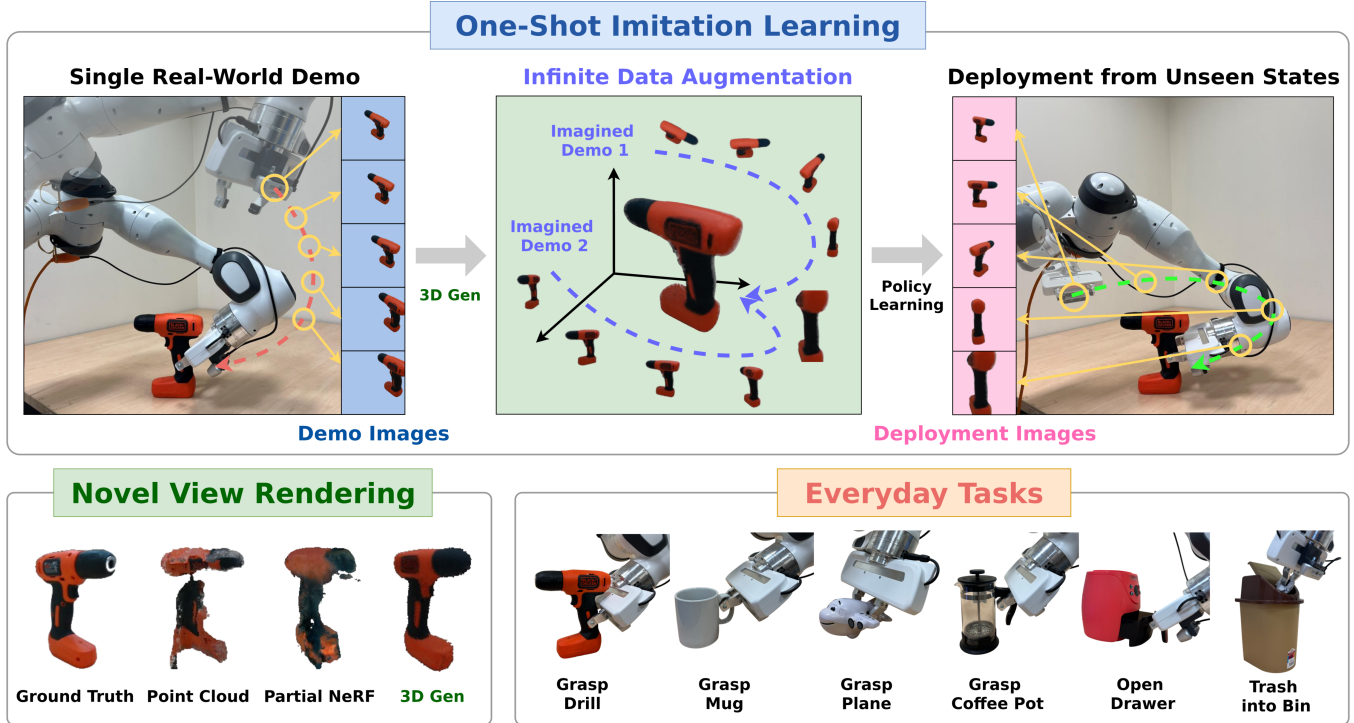


Fig. 1: We utilise 3D generative models for data augmentation to enable one-shot imitation learning from a single demonstration, with end-to-end policies from a wrist-mounted RGB camera. Given a single real-world demonstration, a full 3D model of the object is generated through the generative model, which allows for 3D augmentation of an infinite number of “imagined” demonstrations via novel view rendering. The augmented dataset is then used to train an “omnidirectional” policy, enabling tasks to be executed from any initial state, even if that state is significantly different from any in the real-world demonstration. Leveraging the generalisation and high-quality novel view rendering capabilities of 3D generative models, our method can be applied to multiple everyday tasks.

Abstract—Recent 3D generative models, which are capable of generating full object shapes from just a few images, now open up new opportunities in robotics. In this work, we show that 3D generative models can be used to augment a dataset from a single real-world demonstration, after which an omnidirectional policy can be learned within this imagined dataset. We found that this enables a robot to perform a task when initialised from states very far from those observed during the demonstration, including starting from the opposite side of the object relative to the real-world demonstration, significantly reducing the number of demonstrations required for policy learning. Through several real-world experiments across tasks such as grasping objects, opening a drawer, and placing trash into a bin, we study these omnidirectional policies by investigating the effect of various design choices on policy behaviour, and we show superior performance to recent baselines which use alternative methods for data augmentation. Videos of our experiments can be found on our webpage: <https://www.robot-learning.uk/op-gen>.

I. INTRODUCTION

Demonstrations are a powerful source of data for policy learning, and in recent years, this has led to impressive examples of reactive and dexterous policies [1], [2]. However, typical behavioural cloning methods would likely require hundreds of demonstrations to learn a policy for the tasks in Figure 1. This is because to learn robust omnidirectional policies (OP) — which can succeed from any initial state — the demonstrations must densely cover a very large distribution of states.

In this work, we ask whether these omnidirectional policies can instead be learned from only a single demonstration with a wrist-mounted RGB camera, by bringing in recent 3D generative models [3]. Having been trained on huge datasets of objects, these models enable images to be imagined from any viewpoint of a new object, when given only a small number of images of that object. For example, they can

¹ The Robot Learning Lab at Imperial College London.

produce the “back” of an object when only its “front” is observed. Given real images observed during a single demonstration, we therefore propose that images from novel viewpoints can be imagined and automatically labelled with actions. A policy trained on this “imagined” dataset would then be in-distribution for any view of the object, even if that view is from the opposite side of the object from where the demonstration was collected.

This can be seen as a form of dataset augmentation. Prior works such as DemoGen [4] reconstruct partial point clouds from demonstrations for this purpose, but conventional point cloud methods cannot recover unseen geometry accurately, limiting generalisation when those regions are relevant at test time. Fortunately, with the arrival of 3D generative AI, we now show how full 3D augmentation can be achieved to enable generalisation to viewpoints that were previously entirely unobserved.

We introduce **OP-Gen**: omnidirectional policies through 3D generative models. Similar to [4], we first decompose the single demonstration into *motion* and *skill* phases. Then, we generate a full 3D model of the target object by using wrist-camera images captured during a demonstration. Based on the 3D model, collision-free end-effector (EEF) trajectories as new *motions* could be generated that guide the robot to return to, and then follow, the original *skill*. By rendering synthetic images using the generated object model, we then create a large “imagined” dataset of image-action pairs and use these to train a diffusion policy [5] which is then robust to any initial EEF pose where the object is within the camera’s view.

To the best of our knowledge, this is the first method for 6-DoF policy learning that uses 3D generative models for single-demonstration augmentation from a wrist-mounted RGB camera. Since current 3D generative models are typically designed for single-object generation, in our real-world experiments, we focus on single-object tasks such as grasping objects, opening a drawer, and placing trash into a bin. However, as generative models improve, this method could be extended to full scenes. We show that our omnidirectional policies outperform alternative methods for 3D augmentation, such as rendering images from a point cloud or a NeRF reconstruction. Our ablation studies then explore how the quality of the generated 3D model affects task performance, and we find what the optimal strategy is to generate these imagined datasets when given a single demonstration.

II. RELATED WORK

Efficient Imitation Learning. In robotics, real-world data is sparse and expensive to collect. This makes data-efficient imitation learning crucial, yet current approaches typically require around a hundred demonstrations to train robust policies [5], [6], [7], [8]. Replay-based approaches mitigate this by positioning the robot at a “bottleneck” pose relative to the target object before replaying the demonstrated interactions [9], [10], [11], [12], [13], which enables one-shot imitation learning. With additional self-supervised data collection, [14]

achieves high performance on contact-rich tasks from a single demonstration. Novel in-context learning frameworks further enhance efficiency [15], [16], and recent works even push the boundaries toward zero-shot manipulation [17], [18], [19].

2D Data Augmentation. Data augmentation has traditionally supported 2D domain randomisation through image cropping, flipping, and lighting variations to improve policy robustness [20], [21], [22]. Additionally, works such as [23], [24], [25] focus on augmenting data to reduce the sim-to-real gap. ROSIE [26] extends this by modifying backgrounds and introducing distractors, leveraging text-to-image models [27], [28], [29], [30]. However, none of these techniques enable generalisation to unseen object parts. Our method seamlessly integrates with these approaches, enabling a more comprehensive form of augmentation.

3D Data Augmentation. Given that most robotic tasks operate in 6-DoF spaces, 3D data augmentation provides substantial benefits. SPARTN [31] employs NeRFs [32] to perturb end-effector poses for data augmentation but is limited to nearby views. In contrast, our method uses 3D generative models to fully generate the target object, allowing us to sample arbitrary augmented trajectories. While [33] achieves object-level generalisation with NeRFs and [34] uses diffusion models for future observation prediction even with dynamic interaction, both lack coverage of unseen regions. MimicGen [35] and its variations [36], [37] could generate unlimited demonstrations based on a small number of human demonstrations from simulation but faces sim-to-real gap. To address it, [38] deforms the target object and uses geometry-aware data generation to generalise to both novel poses and geometries, achieving zero-shot sim-to-real transfer. However, all of them require the complete object model. DemoGen [4], on the other hand, collects demos in the real world and augments the demo by transforming the object-level partial point clouds. However, it is difficult to generalise to initial states observing unseen parts of the objects during demonstration. Other real-to-sim transfer [39], [40], [41], [42], [43] methods also require full object geometry and dynamics, which are hard to extract from a single demo. With the recent advances in 3D generation, researchers have begun exploring such methods to address the problem [44]. Similar to our idea, [45] uses zero-shot novel view synthesis to alter demonstration observations to novel virtual camera views, but without augmenting actions. Instead, our method not only augments observations but also synthesises novel, executable actions. RobotTwin [46] also uses 3D generation to generate the complete object model, but the generated expert data is from GPT-4V [47] coding, which may not be feasible in real-world, while we collect it from human demo.

3D vision for robotics. 3D vision is increasingly used in robotics due to its advancements and the natural compatibility with robotic systems. NeRF [32], Instant-NGP [48] and Gaussian Splatting [49] enable efficient, photorealistic novel view synthesis, which enables various downstream applications in robotics [18], [43], [50], [51]. Despite their

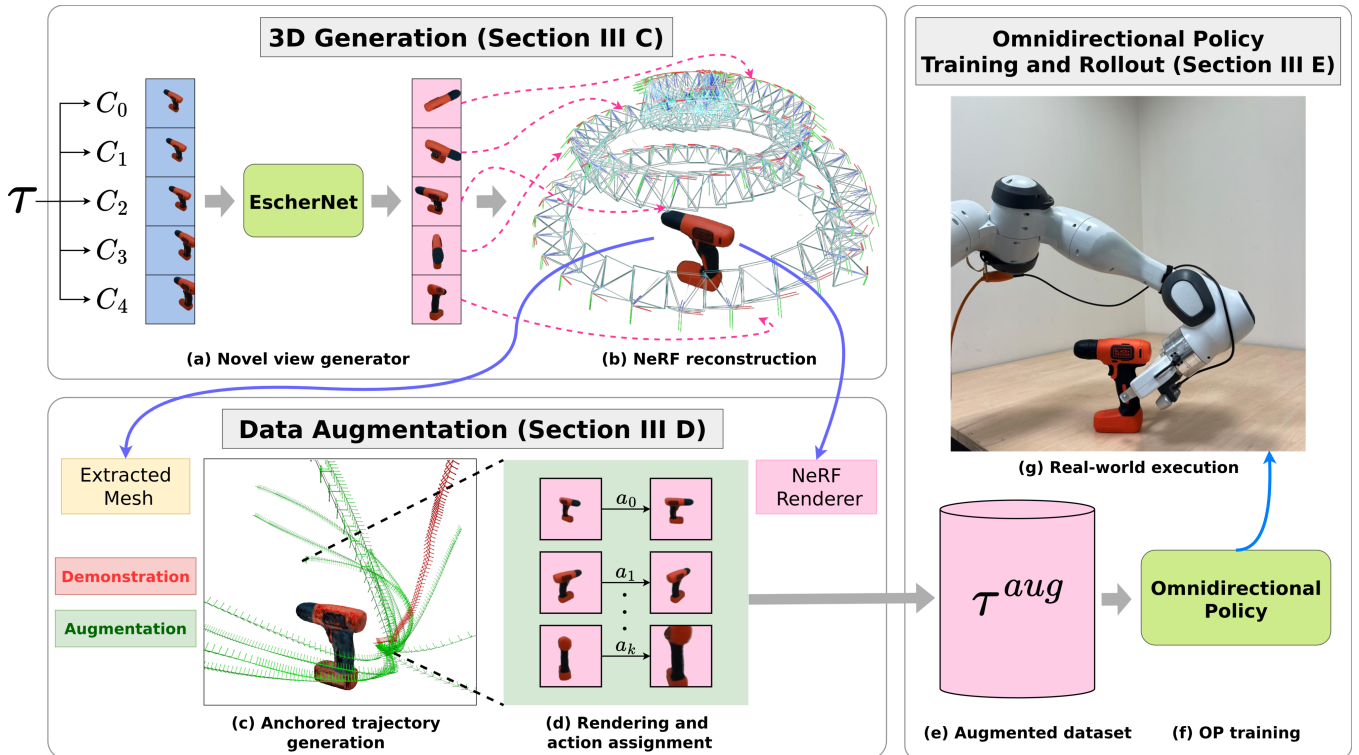


Fig. 2: The OP-Gen pipeline begins with a single demonstration τ , from which posed images are sampled and fed into EscherNet [3] for novel view synthesis (a). The resulting multi-view images are used to construct a NeRF [48] for efficient rendering (b). The extracted 3D mesh of the target object enables our anchored trajectory generation module to create novel trajectories (c). Then we render new observations via the pre-built NeRF and assign corresponding actions (d). These are aggregated into an augmented dataset (e), used to train a diffusion policy [5] (f), which is then deployed in real-world rollouts (g).

success, these approaches require dense view coverage, limiting their usage in sparse or low-data scenarios common in robotics. Recent 3D generative models [52], [53], [54], [55], [56], [57] address this gap by enabling plausible view synthesis and object generation from minimal input, but none of them ensure up-to-scale alignment to the real world. To address this, EscherNet [3] encodes camera poses similar to language models and integrates them with RGB images, achieving any-to-any view synthesis while maintaining scale awareness.

III. OP-GEN: OMNIDIRECTIONAL POLICIES THROUGH 3D GENERATIVE MODELS

A. Overview

From a single demonstration, the target object is only partially observed, making it challenging to perform the task from unseen views. OP-Gen addresses this by using 3D generative models to generate the object and synthesise consistent renderings from unseen viewpoints. These are labeled with actions that guide the robot back to and along the demonstration, enabling training of an omnidirectional policy, as shown in Fig. 2.

B. Single Demonstration

We consider a one-shot, RGB-only imitation learning setting, in which a single demonstration τ is provided for

each task. Each demonstration comprises a sequence of observation-action tuples $\{I_t, C_t, a_t\}$, where I_t denotes a 64×64 RGB image captured from a wrist-mounted camera, C_t represents the corresponding 6-DoF camera pose, and a_t indicates the 7-DoF EEF action. The EEF action consists of a 6-DoF transformation to the next pose relative to the EEF frame and a 1-DoF gripper state (open or close). All pose representations are expressed in angle-axis format. Following the conventions of [4], [9], [11], [12], [35], each demonstration is divided into *motion* and *skill* phases, with “bottleneck” points marking the transitions, which are easily identified by checking if the distance between the EEF and the centre of the target object falls within a threshold. During data augmentation, the *skill* phases are directly transformed as complete segments, whereas the *motion* phases are re-planned using motion planning to bridge consecutive *skill* phases, consistent with [4], [31]. Furthermore, given that current 3D generation techniques primarily address object-level rather than scene-level synthesis, we perform target object segmentation during both training and testing phases using XMem [58], aligning with state-of-the-art practices.

C. 3D Generation

From single-view or few-views inputs, we can synthesise novel views through 3D generative models, which is shown in Fig. 2(a). We use EscherNet [3] as our novel view gener-

ator \mathcal{G} since it can generate up-to-scale 3D consistent novel views. To be specific, for each demonstration τ , we sample 5 images $I_S = \{I_k\}_{k=1}^5$ and their corresponding camera poses $C_S = \{C_k\}_{k=1}^5$ as inputs to EscherNet, and then query renderings from 100 novel views $I_Q = \{\mathcal{G}(I_S, C_S, C_q)\}_{q=1}^{100}$ within a minute, where C_q is the queried pose along an Archimedean spiral centered at the object as shown in Fig. 2(b). While EscherNet can render images directly, querying it repeatedly during data augmentation is computationally expensive and time consuming. As a result, we build a NeRF based on the rendered images I_Q using Instant-NGP [48] for faster rendering. In addition, we extract the mesh of the object \mathcal{M}_O from Instant-NGP for subsequent collision checking.

D. Data Augmentation

By leveraging the NeRF model, we are able to render images from arbitrary sampled viewpoints within the virtual environment. Moreover, given access to the mesh of the target object, we generate complete, collision-free trajectories from any sampled viewpoint back to the demonstration trajectory, rather than subtly perturbing demonstration actions as in [31]. However, in the absence of explicit constraints to ensure that the camera remains focused on the target object, the rendered images may include irrelevant or blank regions, potentially degrading policy performance. To address this, we propose an Anchored Trajectory Generation (ATG) pipeline, as illustrated in Fig. 3.

Anchored Trajectory Generation. First, as shown in Fig.3(a), an EEF trajectory $\{E_i\}_{i=1}^k$ is generated from a randomly sampled pose to the predefined bottleneck pose using CuRobo [59], a parallelised, collision-free motion planner, where each E_i represents a 6-DoF EEF pose. Subsequently, anchor points are uniformly sampled along this trajectory, as denoted by S_{ap} in Fig.3(b). For each anchor point, we fix its position while adjusting its orientation to ensure that the camera remains focused on the target object. To enhance generalisation, small perturbations are added to the orientation, resulting in corrected poses E_i^{correct} . We refer to this adjustment process as re-focus, illustrated in Fig.3(c). Finally, to ensure smooth rotational transitions between consecutive anchor points, the start and end points, we apply spherical linear interpolation (SLERP), yielding the augmented anchored trajectory $\{E_i^{\text{aug}}\}_{i=1}^k$, depicted in Fig.3(d).

Rendering and Action Assignment. After acquiring the anchored trajectories, the corresponding augmented camera poses $\{C_i^{\text{aug}}\}_{i=1}^k$ are computed using the pre-calibrated camera-to-EEF transformation. These new camera poses are then used to render images $\{I_i^{\text{aug}}\}_{i=1}^k$ as novel observations via the pre-built NeRF model. Meanwhile, for each EEF pose along the trajectory, we compute the relative transformation to the subsequent pose $E_i^{-1}E_{i+1}$, and integrate it with the gripper state to form the new action set $\{a_i^{\text{aug}}\}_{i=1}^k$. The gripper state is assigned a value of 1 (close) only when the pose is within 1 cm of the bottleneck. Since fewer than 1% of augmented poses are near the bottleneck, we oversample

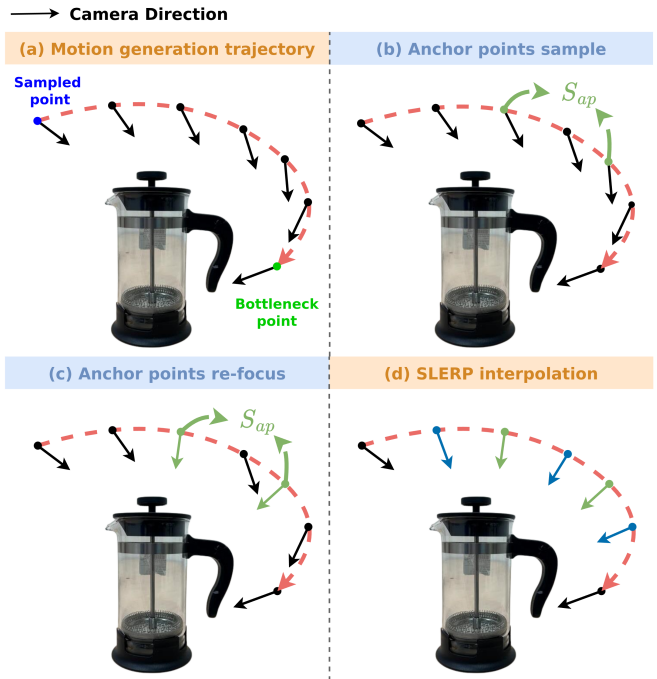


Fig. 3: An illustration of how anchored trajectory generation works. (a) shows the generated collision-free trajectory, and the black arrows are the look-at directions of the cameras. Note we always fix the poses of the sampled starting point and the last bottleneck point afterward; (b) shows the evenly sampled anchor points; (c) shows the re-focus process; (d) shows the final SLERP interpolation.

poses within 1 cm of it to ensure balanced data distribution. Finally, by associating anchored trajectories, we construct the augmented dataset $\mathcal{D}_{\text{aug}} = \{I_i^{\text{aug}}, C_i^{\text{aug}}, a_i^{\text{aug}}\}_{i=1}^K$, where $K = k_1 + k_2 + \dots + k_n$ denotes the total number of generated data points. In practice, we set $K = 20000$.

E. Training and Policy Rollout

After obtaining the augmented dataset, we train a behavioural cloning (BC) policy to mimic actions in it. The objective is to optimise a policy π_θ that closely fits the augmented data. Specifically, we adopt diffusion policy [5] as the backbone for our approach, thus the training loss is formulated as

$$\mathcal{L} = \text{MSE}(\epsilon^k, \epsilon_\theta(I_t, a_t + \epsilon^k, k)), \quad (1)$$

where ϵ_θ represents the diffusion model used to predict the added noise at each step k . During testing, we predict the relative EEF pose by iteratively denoising randomly initialised actions using the DDIM algorithm [60]. Specifically, we use ResNet18 [61] as our visual backbone and we set the observation horizon to 1 and the action horizon to 4. Also, we set training diffusion steps to 100 and inference diffusion steps to 16. After 100000 global training steps, we select the model with the lowest validation loss as the final policy.

IV. EXPERIMENTS

A. Experimental Setup

In this section, we evaluate our data augmentation method in a one-shot imitation learning setting. Specifically, we conduct experiments on 6 different real-world tasks: *drill*, *mug*, *plane* and *coffee pot* grasping, placing trash into a *trash bin*, and opening the air fryer *drawer*, as shown in Figure 1. For each task, we collect only one demonstration trajectory of approximately 10 seconds, including an RGB sequence with the corresponding EEF poses and gripper states at 20Hz. Then we augment the original dataset to a total of 20000 data points and train our omnidirectional policy using the augmented dataset. Lastly, we test the rollout policies in both simulation and the real world.

Simulation. To quantitatively measure the policy performance, we create a visual simulator for each task using Instant-NGP [48]. In detail, apart from the single demonstration, we scan the whole object from a hemispherical camera trajectory which contains about 600 posed RGB images, and build a full NeRF of the scene based on them, serving as the visual simulator. To define task success, we measure the remaining distance to the bottleneck point when the policy commands to execute the *skill* phase. The task is considered successful if this to-go distance is less than 1 cm.

Real world. We employ a 7-DoF Franka Panda equipped with a wrist-mounted Intel RealSense D435 RGB-D camera. Note that since our method is RGB only, the depth images are only used for another baseline. For all the grasping tasks, we define success when the robot manages to grasp and lift the target object for at least 5s. For the trash into bin task, we define success when the trash paper is placed in the bin. For the opening drawer of air fryer task, we define success when the drawer of air fryer is opened by the gripper.

B. Can OP-Gen solve a range of everyday tasks from a single demonstration and how does it compare to baselines?

We evaluate our data augmentation scheme on six real-world tasks, conducting 20 rollouts per task using four different baselines. During each rollout, the EEF starts at different poses sampled from the working space. Among these, 10 initial poses are sampled within a $\pm 45^\circ$ fan-shaped range around the object, with the central axis aligned to the first demo camera view. These poses are categorised as **Narrow** initial poses, while the remaining poses sampled outside this range are categorised as **Omni** initial poses. We compare our OP-Gen with baselines including: (1) **No Aug**: single demonstration without augmentation. This represents the lower bound of the method. (2) **OP-PCD**: we reconstruct a partial point cloud of the target object using RGB-D images from the single demonstration. For best practice, we remove points that are further away from their neighbors on average. Then we project point clouds onto 2D images rather than rendering from our 3D generation module. Comparison with this baseline will show the benefits of using complete 3D generation rather than partial reconstruction. (3) **SPARTN**: we use our implementation of SPARTN [31], which builds

a partial NeRF using camera views along the demonstration trajectory. Then we augment the dataset as our main method. This method can provide plausible data augmentation near the demonstration views but no additional information from the unseen part of the object. (4) **Upper Bound (UB)**: full NeRF based augmentation. We replace our 3D generation module with the previous full-scan NeRF of the object. Note that since we’re investigating one-shot imitation learning, demonstration views will be inadequate for the full NeRF training. As a result, we only consider this method as an upper bound rather than a fair baseline. To highlight the data efficiency of our method, we also record the data collection time for each of the baseline methods.

All real-world experiment results are summarised in Table I. Across all methods, performance in the **Narrow** setting consistently surpasses that in the **Omni** setting. Without any data augmentation, policies fail during all rollouts due to out-of-distribution states, confirming that a single demonstration is insufficient for effective behavioural cloning. Augmentation via OP-PCD slightly improves performance, but due to a significant rendering gap as shown in Fig. 4, the resulting policy handles fewer than half of the initial poses, achieving only an 18.3% average success rate in the **Narrow** setting and 5% in the **Omni** setting. SPARTN’s partial NeRF reconstruction yields a 28.3% success rate in the **Narrow** setting but still fails in most **Omni** cases, due to missing information from novel viewpoints. In contrast, our proposed method achieves an average success rate of 85% from the **Narrow** regions and 73.3% from the **Omni** regions, significantly outperforming all baselines and approaching the performance of the upper bound. Notably, our method maintains similar performance across both settings, demonstrating that 3D generative models can provide informative representations even under drastic viewpoint changes. During testing, we observed that nearly all failure cases stemmed from last-inch inaccuracies—either due to premature gripper command or collisions. We attribute these errors to subtle misalignments between the generated 3D model and the physical object, as well as a limited number of grasp action labels, leading to a multi-modal distribution in the final EEF action predictions. Overall, these results demonstrate that 3D generative models serve as effective tools for data augmentation, enhancing the robustness of behavioural cloning policies. Additionally, they contribute valuable information beyond the original demonstration distribution, substantially reducing the need for large amounts of real-world training data.

C. How critical is 3D generation quality for OP-Gen?

To evaluate the impact of the 3D generation model on policy performance, we present qualitative comparisons of novel view renderings produced by different baselines in Fig. 4. As shown, the UB generates renderings that are nearly identical to the ground truth (GT), thereby supporting strong omnidirectional policy performance. Our proposed OP-Gen also produces renderings that are visually similar to the GT, maintaining sufficient fidelity for effective policy training. In contrast, renderings from SPARTN and OP-PCD

TABLE I: Success rates for OP-Gen and 4 baselines across 6 real-world tasks (%), as well as the corresponding data collection time (s). 10 rollouts each in both Narrow and Omni settings.

Level	Narrow							Omni							Total Avg	Time(s)
	Drill	Mug	Plane	Coffee	Bin	Fryer	Avg	Drill	Mug	Plane	Coffee	Bin	Fryer	Avg		
No Aug	0	0	0	0	0	0	0.0	0	0	0	0	0	0	0.0	0.00	10
OP-PCD	0	0	30	20	40	20	18.3	0	0	0	0	20	10	5.0	11.65	10
SPARTN	20	20	30	30	60	10	28.3	0	20	0	0	0	0	3.3	15.80	10
OP-Gen	90	90	70	90	80	90	85.0	90	60	80	60	80	70	73.3	79.15	10
UB	90	90	80	80	80	90	85.0	100	80	80	80	80	80	83.3	84.15	90

deviate significantly from the GT, lacking even structural correspondence when changing to the opposite of the input views, which hampers the methods’ ability to learn OP effectively from these views.

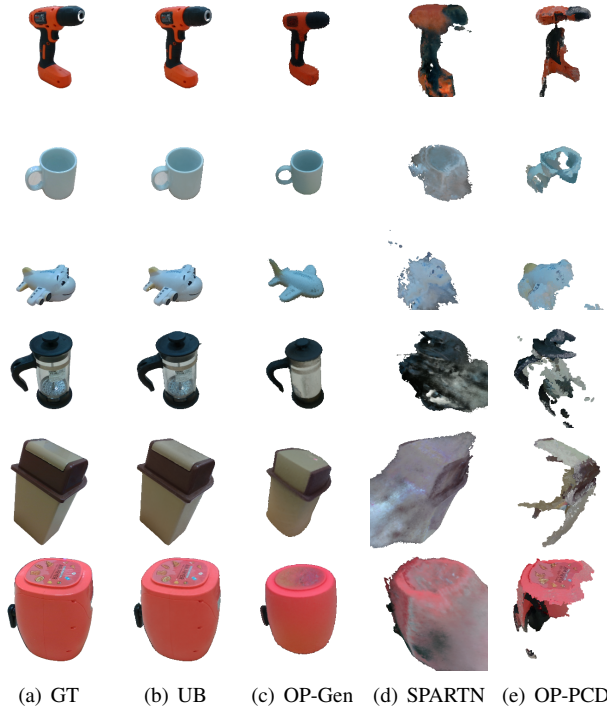


Fig. 4: Qualitative results showing renders from different novel views across all methods.

To quantitatively evaluate the impact of 3D generation and reconstruction quality, we measure the average SSIM [62] scores between renderings and GT images along the full NeRF scan trajectory across all methods, reflecting their structural similarity. Fig. 5 illustrates how SSIM affects the success rate. As shown, full-scan UB consistently achieves the highest SSIM and success rates, establishing it as the upper bound for OP learning. Our OP-Gen method, utilising EscherNet [3], attains comparable success within the SSIM range of 0.8 – 0.95. However, SPARTN and OP-PCD achieve less than 30% success despite SSIM values ranging from 0.7 to 0.95. Although these ranges overlap, most SSIM values for SPARTN and OP-PCD cluster between 0.7 and 0.85, with only the *mug* and *plane* tasks reaching higher SSIM values. This exception is due to the textureless surfaces

of these objects, which simplify reconstruction. Meanwhile, OP-Gen consistently achieves SSIM between 0.85 and 0.95 across tasks, leaving only two large complex objects *bin* and *air fryer* out of range, reflecting the increased difficulty of accurate reconstruction. Based on these observations, we conclude that an SSIM above 0.95 is necessary for small, textureless objects to achieve high policy performance, while an SSIM above 0.8 suffices for larger, more complex objects.

Across tasks, we also observe a correlation between higher SSIM scores and increased policy success rates. Interestingly, when SSIM falls below 0.95, it becomes important to examine the consistency between views. For instance, OP-PCD and SPARTN achieve SSIM around 0.95 near the input angles but drop below 0.5 when rendering from opposite directions, making object structure unrecognizable as in Fig. 4. In contrast, OP-Gen maintains consistent SSIM around 0.85 across all viewpoints, enabling reliable object identification. Therefore, while higher image fidelity improves policy performance, consistency across viewpoints is even more crucial for omnidirectional policy learning.

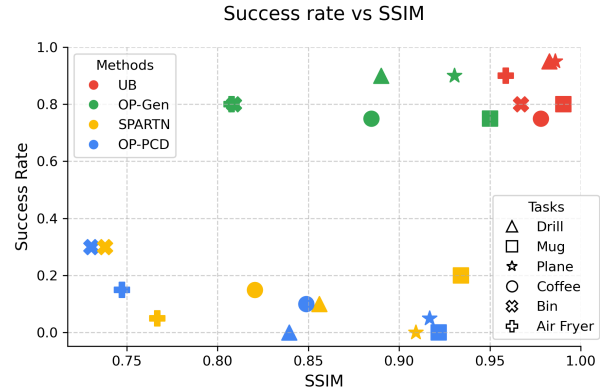


Fig. 5: Relationship between task success rate and SSIM value across different tasks and baselines.

D. How would different trajectory generation pipelines affect the performance?

To assess each component’s impact in the anchored trajectory generation pipeline, we conduct an ablation study across six tasks. We systematically remove components or introduce variations and report the average to-go distance to the bottleneck in simulation, as well as average success rates in both simulation and real-world settings. As shown in Table II, we ablate four implementations. First, removing the view re-focus (w/o VRF) module significantly reduces

performance, as objects may leave the camera’s view, leading to ineffective datasets. Second, using only motion planning (MP only), without VRF or SLERP interpolation, yields a 46.67% real-world success rate, suggesting SLERP adds subtle view-focusing constraints. Third, applying VRF at all motion-planned trajectory points without SLERP (MP + VRF) drops the success rate to 4.17% due to abrupt rotations, especially near the trajectory center, resulting in unstable action labels. Lastly, a linear variant (Linear) without collision-free planning achieves a 43.33% real-world success rate, with most failures attributed to collisions. Since the simulator lacks collision checking, this variant shows artificially lower to-go distances and inflated simulated success.

TABLE II: Ablation study on different building blocks for anchored trajectory generation.

Method	Simulation Dist	Simulation SR	Real World SR
OP	0.013	83.33	79.17
w/o VRF	0.082	80.83	53.33
MP only	0.152	75	46.67
MP + VRF	0.123	6.67	4.17
Linear	0.009	95	43.33

V. CONCLUSION

We presented OP-Gen, which turns a single wrist-camera demonstration into a large, omnidirectional training set using 3D generative models. From six real-world manipulation tasks, three lessons emerge. First, the learned omnidirectional policies succeed from multiple unseen initial states, clearly outperforming point-cloud and partial-NeRF baselines and approaching a full-scan upper bound, demonstrating that 3D generative models provide promising data augmentation. Second, while higher-quality novel-view renderings help, the consistency across viewpoints is more critical for omnidirectional policy learning. Finally, ablations show the anchored-trajectory pipeline is essential, and removing it markedly reduces real-world success. Overall, 3D generative models provide a practical route to 3D data augmentation for one-shot imitation learning, and continued advances in 3D generation should further strengthen omnidirectional policy robustness and generalisation.

VI. LIMITATIONS

We identify several limitations to be addressed in future work. Our method relies heavily on the quality of 3D generative models, which themselves are still limited. As demonstrated by our evaluation of how 3D generation quality affects OP-Gen’s performance, high-fidelity novel view renderings and cross-view consistency are critical for effective omnidirectional policy learning.

Furthermore, because reliable scene-level generation is lacking, we restrict augmentation to the object level via segmentation. Thus, test-time success partly depends on segmentation accuracy. Nevertheless, we are optimistic that, as more accurate 3D generation models continue to emerge, the effectiveness of our approach will correspondingly improve.

In addition, since the augmentation is instance-specific, the current method does not generalise to novel objects. However, additional 2D augmentation (e.g., replacing the target object with variants) may enable cross-object generalisation.

Finally, our present method does not augment the dynamic interaction of demonstrations, which remains an open challenge in robot learning from a single demonstration. However, in the future, techniques such as video generation or real-to-sim could potentially address this limitation.

REFERENCES

- [1] K. Black, N. Brown, D. Driess, A. Esmail, M. Equi, C. Finn, N. Fusai, L. Groom, K. Hausman, B. Ichter *et al.*, “ π_0 : A vision-language-action flow model for general robot control,” *arXiv preprint arXiv:2410.24164*, 2024.
- [2] T. Z. Zhao, J. Tompson, D. Driess, P. Florence, K. Ghasemipour, C. Finn, and A. Wahid, “Aloha unleashed: A simple recipe for robot dexterity,” *arXiv preprint arXiv:2410.13126*, 2024.
- [3] X. Kong, S. Liu, X. Lyu, M. Taher, X. Qi, and A. J. Davison, “Eschernet: A generative model for scalable view synthesis,” in *Proceedings of the IEEE/CVF Conference on Computer Vision and Pattern Recognition*, 2024, pp. 9503–9513.
- [4] Z. Xue, S. Deng, Z. Chen, Y. Wang, Z. Yuan, and H. Xu, “Demogen: Synthetic demonstration generation for data-efficient visuomotor policy learning,” *arXiv preprint arXiv:2502.16932*, 2025.
- [5] C. Chi, Z. Xu, S. Feng, E. Cousineau, Y. Du, B. Burchfiel, R. Tedrake, and S. Song, “Diffusion policy: Visuomotor policy learning via action diffusion,” *The International Journal of Robotics Research*, p. 02783649241273668, 2023.
- [6] H. Bharadhwaj, J. Vakil, M. Sharma, A. Gupta, S. Tulsiani, and V. Kumar, “Roboagent: Generalization and efficiency in robot manipulation via semantic augmentations and action chunking,” in *2024 IEEE International Conference on Robotics and Automation (ICRA)*. IEEE, 2024, pp. 4788–4795.
- [7] E. Jang, A. Irpan, M. Khansari, D. Kappler, F. Ebert, C. Lynch, S. Levine, and C. Finn, “Bc-z: Zero-shot task generalization with robotic imitation learning,” in *Conference on Robot Learning*. PMLR, 2022, pp. 991–1002.
- [8] T. Z. Zhao, V. Kumar, S. Levine, and C. Finn, “Learning fine-grained bimanual manipulation with low-cost hardware,” *arXiv preprint arXiv:2304.13705*, 2023.
- [9] E. Johns, “Coarse-to-fine imitation learning: Robot manipulation from a single demonstration,” in *IEEE International Conference on Robotics and Automation (ICRA)*, 2021.
- [10] E. Valassakis, G. Papagiannis, N. Di Palo, and E. Johns, “Demonstrate once, imitate immediately (dome): Learning visual servoing for one-shot imitation learning,” in *2022 IEEE/RSJ International Conference on Intelligent Robots and Systems (IROS)*. IEEE, 2022, pp. 8614–8621.
- [11] P. Vitiello, K. Dreczkowski, and E. Johns, “One-shot imitation learning: A pose estimation perspective,” *arXiv preprint arXiv:2310.12077*, 2023.
- [12] B. Wen, W. Lian, K. Bekris, and S. Schaal, “You only demonstrate once: Category-level manipulation from single visual demonstration,” *arXiv preprint arXiv:2201.12716*, 2022.
- [13] N. Di Palo and E. Johns, “On the effectiveness of retrieval, alignment, and replay in manipulation,” *IEEE Robotics and Automation Letters*, vol. 9, no. 3, pp. 2032–2039, 2024.
- [14] G. Papagiannis and E. Johns, “Miles: Making imitation learning easy with self-supervision,” in *Proceedings of the Conference on Robot Learning (CoRL)*, 2024.
- [15] N. Di Palo and E. Johns, “Keypoint action tokens enable in-context imitation learning in robotics,” in *Proceedings of Robotics: Science and Systems (RSS)*, 2024.
- [16] V. Vosylius and E. Johns, “Instant policy: In-context imitation learning via graph diffusion,” *arXiv preprint arXiv:2411.12633*, 2024.
- [17] I. Kapelyukh, V. Vosylius, and E. Johns, “Dall-e-bot: Introducing web-scale diffusion models to robotics,” *IEEE Robotics and Automation Letters*, vol. 8, no. 7, pp. 3956–3963, 2023.
- [18] I. Kapelyukh, Y. Ren, I. Alzugaray, and E. Johns, “Dream2Real: Zero-shot 3D object rearrangement with vision-language models,” in *IEEE International Conference on Robotics and Automation (ICRA)*, 2024.

- [19] T. Kwon, N. Di Palo, and E. Johns, "Language models as zero-shot trajectory generators," *IEEE Robotics and Automation Letters*, 2024.
- [20] M. Laskin, K. Lee, A. Stooke, L. Pinto, P. Abbeel, and A. Srinivas, "Reinforcement learning with augmented data," *Advances in neural information processing systems*, vol. 33, pp. 19 884–19 895, 2020.
- [21] B. Li, V. François-Lavet, T. Doan, and J. Pineau, "Domain adversarial reinforcement learning," *arXiv preprint arXiv:2102.07097*, 2021.
- [22] D. Yarats, I. Kostrikov, and R. Fergus, "Image augmentation is all you need: Regularizing deep reinforcement learning from pixels," in *International conference on learning representations*, 2021.
- [23] D. Ho, K. Rao, Z. Xu, E. Jang, M. Khansari, and Y. Bai, "Retinagan: An object-aware approach to sim-to-real transfer," in *2021 IEEE International Conference on Robotics and Automation (ICRA)*. IEEE, 2021, pp. 10 920–10 926.
- [24] K. Rao, C. Harris, A. Irpan, S. Levine, J. Ibarz, and M. Khansari, "RI-cyclegan: Reinforcement learning aware simulation-to-real," in *Proceedings of the IEEE/CVF Conference on Computer Vision and Pattern Recognition*, 2020, pp. 11 157–11 166.
- [25] F. Sadeghi, A. Toshev, E. Jang, and S. Levine, "Sim2real view invariant visual servoing by recurrent control," *arXiv preprint arXiv:1712.07642*, 2017.
- [26] T. Yu, T. Xiao, A. Stone, J. Tompson, A. Brohan, S. Wang, J. Singh, C. Tan, J. Peralta, B. Ichter *et al.*, "Scaling robot learning with semantically imagined experience," *arXiv preprint arXiv:2302.11550*, 2023.
- [27] A. Ramesh, M. Pavlov, G. Goh, S. Gray, C. Voss, A. Radford, M. Chen, and I. Sutskever, "Zero-shot text-to-image generation," in *International conference on machine learning*. Pmlr, 2021, pp. 8821–8831.
- [28] A. Ramesh, P. Dhariwal, A. Nichol, C. Chu, and M. Chen, "Hierarchical text-conditional image generation with clip latents," *arXiv preprint arXiv:2204.06125*, vol. 1, no. 2, p. 3, 2022.
- [29] R. Rombach, A. Blattmann, D. Lorenz, P. Esser, and B. Ommer, "High-resolution image synthesis with latent diffusion models," in *Proceedings of the IEEE/CVF conference on computer vision and pattern recognition*, 2022, pp. 10 684–10 695.
- [30] K. Saharia, W. Chan, S. Saxena, L. Li, J. Whang, E. L. Denton, C. Ghasemipour, R. Gontijo Lopes, B. Karagol Ayan, T. Salimans *et al.*, "Photorealistic text-to-image diffusion models with deep language understanding," *Advances in neural information processing systems*, vol. 35, pp. 36 479–36 494, 2022.
- [31] A. Zhou, M. J. Kim, L. Wang, P. Florence, and C. Finn, "Nerf in the palm of your hand: Corrective augmentation for robotics via novel-view synthesis," in *Proceedings of the IEEE/CVF Conference on Computer Vision and Pattern Recognition*, 2023, pp. 17 907–17 917.
- [32] B. Mildenhall, P. P. Srinivasan, M. Tancik, J. T. Barron, R. Ramamoorthi, and R. Ng, "Nerf: Representing scenes as neural radiance fields for view synthesis," *Communications of the ACM*, vol. 65, no. 1, pp. 99–106, 2021.
- [33] E. Zhu, M. Levy, M. Gwilliam, and A. Shrivastava, "Nerf-aug: Data augmentation for robotics with neural radiance fields," *arXiv preprint arXiv:2411.02482*, 2024.
- [34] X. Zhang, M. Chang, P. Kumar, and S. Gupta, "Diffusion meets dagger: Supercharging eye-in-hand imitation learning," *arXiv preprint arXiv:2402.17768*, 2024.
- [35] A. Mandlekar, S. Nasiriany, B. Wen, I. Akinola, Y. Narang, L. Fan, Y. Zhu, and D. Fox, "Mimicgen: A data generation system for scalable robot learning using human demonstrations," *arXiv preprint arXiv:2310.17596*, 2023.
- [36] C. Garrett, A. Mandlekar, B. Wen, and D. Fox, "Skillmimicgen: Automated demonstration generation for efficient skill learning and deployment," *arXiv preprint arXiv:2410.18907*, 2024.
- [37] Z. Jiang, Y. Xie, K. Lin, Z. Xu, W. Wan, A. Mandlekar, L. Fan, and Y. Zhu, "Dexmimicgen: Automated data generation for bimanual dexterous manipulation via imitation learning," *arXiv preprint arXiv:2410.24185*, 2024.
- [38] K. Lin, V. Rangunath, A. McAlinden, A. Prasad, J. Wu, Y. Zhu, and J. Bohg, "Constraint-preserving data generation for visuomotor policy learning," *arXiv preprint arXiv:2508.03944*, 2025.
- [39] M. Torne, A. Simeonov, Z. Li, A. Chan, T. Chen, A. Gupta, and P. Agrawal, "Reconciling reality through simulation: A real-to-sim-to-real approach for robust manipulation," *arXiv preprint arXiv:2403.03949*, 2024.
- [40] J. Kerr, C. M. Kim, M. Wu, B. Yi, Q. Wang, K. Goldberg, and A. Kanazawa, "Robot see robot do: Imitating articulated object manipulation with monocular 4d reconstruction," *arXiv preprint arXiv:2409.18121*, 2024.
- [41] X. Han, M. Liu, Y. Chen, J. Yu, X. Lyu, Y. Tian, B. Wang, W. Zhang, and J. Pang, "Re³sim: Generating high-fidelity simulation data via 3d-photorealistic real-to-sim for robotic manipulation," *arXiv preprint arXiv:2502.08645*, 2025.
- [42] S. Yang, W. Yu, J. Zeng, J. Lv, K. Ren, C. Lu, D. Lin, and J. Pang, "Novel demonstration generation with gaussian splatting enables robust one-shot manipulation," *arXiv preprint arXiv:2504.13175*, 2025.
- [43] L. Barcellona, A. Zadaianchuk, D. Allegro, S. Papa, S. Ghidoni, and E. Gavves, "Dream to manipulate: Compositional world models empowering robot imitation learning with imagination," *arXiv preprint arXiv:2412.14957*, 2024.
- [44] F. Nolte, B. Schölkopf, and I. Posner, "Is single-view mesh reconstruction ready for robotics?" *arXiv preprint arXiv:2505.17966*, 2025.
- [45] S. Tian, B. Wulfe, K. Sargent, K. Liu, S. Zakharov, V. Guizilini, and J. Wu, "View-invariant policy learning via zero-shot novel view synthesis," *arXiv preprint arXiv:2409.03685*, 2024.
- [46] Y. Mu, T. Chen, S. Peng, Z. Chen, Z. Gao, Y. Zou, L. Lin, Z. Xie, and P. Luo, "Robotwin: Dual-arm robot benchmark with generative digital twins (early version)," in *European Conference on Computer Vision*. Springer, 2024, pp. 264–273.
- [47] "Gpt-4v(ision) system card," 2023.
- [48] T. Müller, A. Evans, C. Schied, and A. Keller, "Instant neural graphics primitives with a multiresolution hash encoding," *ACM transactions on graphics (TOG)*, vol. 41, no. 4, pp. 1–15, 2022.
- [49] B. Kerbl, G. Kopanas, T. Leimkühler, and G. Drettakis, "3d gaussian splatting for real-time radiance field rendering," *ACM Trans. Graph.*, vol. 42, no. 4, pp. 139–1, 2023.
- [50] J. Abou-Chakra, K. Rana, F. Dayoub, and N. Stünderhauf, "Physically embodied gaussian splatting: A realtime correctable world model for robotics," *arXiv preprint arXiv:2406.10788*, 2024.
- [51] M. Ji, R.-Z. Qiu, X. Zou, and X. Wang, "Graspsplats: Efficient manipulation with 3d feature splatting," *arXiv preprint arXiv:2409.02084*, 2024.
- [52] R. Liu, R. Wu, B. Van Hoorick, P. Tokmakov, S. Zakharov, and C. Vondrick, "Zero-1-to-3: Zero-shot one image to 3d object," in *Proceedings of the IEEE/CVF international conference on computer vision*, 2023, pp. 9298–9309.
- [53] Y. Liu, C. Lin, Z. Zeng, X. Long, L. Liu, T. Komura, and W. Wang, "Syncdreamer: Generating multiview-consistent images from a single-view image," *arXiv preprint arXiv:2309.03453*, 2023.
- [54] X. Long, Y.-C. Guo, C. Lin, Y. Liu, Z. Dou, L. Liu, Y. Ma, S.-H. Zhang, M. Habermann, C. Theobalt *et al.*, "Wonder3d: Single image to 3d using cross-domain diffusion," in *Proceedings of the IEEE/CVF Conference on Computer Vision and Pattern Recognition*, 2024, pp. 9970–9980.
- [55] V. Voleti, C.-H. Yao, M. Boss, A. Letts, D. Pankratz, D. Tochilkin, C. Laforte, R. Rombach, and V. Jampani, "Sv3d: Novel multi-view synthesis and 3d generation from a single image using latent video diffusion," in *European Conference on Computer Vision*. Springer, 2025, pp. 439–457.
- [56] L. Melas-Kyriazi, I. Laina, C. Rupprecht, and A. Vedaldi, "Realfusion: 360deg reconstruction of any object from a single image," in *Proceedings of the IEEE/CVF conference on computer vision and pattern recognition*, 2023, pp. 8446–8455.
- [57] R. Shi, H. Chen, Z. Zhang, M. Liu, C. Xu, X. Wei, L. Chen, C. Zeng, and H. Su, "Zero123++: a single image to consistent multi-view diffusion base model," *arXiv preprint arXiv:2310.15110*, 2023.
- [58] H. K. Cheng and A. G. Schwing, "Xmem: Long-term video object segmentation with an atkinson-shiffrin memory model," in *European Conference on Computer Vision*. Springer, 2022, pp. 640–658.
- [59] B. Sundaralingam, S. K. S. Hari, A. Fishman, C. Garrett, K. Van Wyk, V. Blukis, A. Millane, H. Oleynikova, A. Handa, F. Ramos *et al.*, "Curobo: Parallelized collision-free minimum-jerk robot motion generation," *arXiv preprint arXiv:2310.17274*, 2023.
- [60] J. Song, C. Meng, and S. Ermon, "Denosing diffusion implicit models," *arXiv preprint arXiv:2010.02502*, 2020.
- [61] K. He, X. Zhang, S. Ren, and J. Sun, "Deep residual learning for image recognition," in *Proceedings of the IEEE conference on computer vision and pattern recognition*, 2016, pp. 770–778.
- [62] Z. Wang, A. C. Bovik, H. R. Sheikh, and E. P. Simoncelli, "Image quality assessment: from error visibility to structural similarity," *IEEE transactions on image processing*, vol. 13, no. 4, pp. 600–612, 2004.